MATERIALS SCIENCE

Air plastron–enabled heat management for enhanced photothermal actuation in underwater soft robots

Pengju Shi†, Chi Chen†*, Zhuo Wang, Wen Hong, Sidi Duan, Zixiao Liu, Wenhao Hou, Muqing Si, Chuan Wei Zhang, Ximin He*

Photothermal self-excited actuators, offering untethered power and control, are promising for autonomous soft robots. While most efforts focus on enhancing heat absorption for greater actuation performance, managing heat dissipation remains underexplored, which becomes critical in underwater environments with rapid convective cooling. Inspired by amphibious mammals that use air plastrons for thermal insulation, we develop a strategy incorporating superhydrophobic candle soot coating to trap air on photothermal liquid crystal elastomer (LCE) actuators. This approach substantially improves thermal insulation underwater, enhances internal temperature gradient, and causes a 282-fold increase in calculated work output. Moreover, we reveal a previously unreported self-oscillation mechanism based on total internal reflection enabled by air plastron, which decouples the locomotion direction from the light incidence direction. Leveraging the enhanced output and maneuverability, we demonstrate LCE-based robots capable of self-continuous locomotion underwater and on water surfaces, powered by overhead or horizontal light, paving the way for next-generation untethered high-performance aquatic soft robots.

INTRODUCTION

Photothermally responsive materials, such as liquid crystal elastomers (LCEs) (*1*, *2*), hydrogels (*3*, *4*), and materials with high coefficients of thermal expansion (*5*, *6*), have drawn widespread attention because of their ability to undergo physical or chemical changes to achieve substantial reconfiguration when exposed to light. These materials are promising for a variety of applications, spanning from self-healing materials (*7*–*10*), tunable optical devices (*11*–*14*), biomedicine (*15*, *16*), and solar energy harvesting (*17*–*19*). Moreover, their shape-morphing properties, remotely controlled by a light source, make them a promising candidate for flexible actuators in soft robotics (*20*–*22*). These light-driven systems offer distinct advantages, including wireless control, programmability, and adaptability, making them ideal for a diverse range of applications, including artificial muscles (*23*–*25*), soft grippers (*26*–*29*), smart switches (*30*, *31*), and locomotive devices (*32*–*35*). Despite their potential, current photothermally driven soft robotic systems face critical challenges, particularly in achieving high actuation speeds and magnitudes (*21*). Therefore, a deeper understanding of the heat transfer process during photothermal actuation is critical, which typically involves the absorption of incident light by photothermal agents and the dissipation of heat into the surrounding environment. For photothermal actuators, an insufficient thermal gradient within the bulk material would limit the thermal strain differences, leading to reduced actuation stroke (*36*). This obstacle becomes especially prominent in demanding yet realistic environments like water. Despite many attempts to develop aquatic untethered soft robots, current designs remain far from real-world applications because of insufficient output and strict light control, which typically requires alignment between the light incidence direction and the locomotion direction beneath the water surface (*37*). Specifically, the high heat conductivity, high density, and high heat capacity of water as a low-temperature reservoir result in substantially greater heat diffusivity compared to air, thereby enhancing both conduction and convection processes, leading to more efficient heat dissipation in underwater environments (*38*). As such environments prevent the heat build-up in the thermally driven actuator, it becomes more difficult to reach the required temperature for deformation (*39*). In other words, for aquatic photothermal actuators, it is crucial to achieve a balance between heat absorption and dissipation rates to enhance the internal thermal gradient, thereby maximizing the power density and overall performance. To achieve this goal, most research nowadays has focused on improving heat absorption efficiency, e.g., by developing photothermal agents with higher absorbance or better compatibility with the host matrix for higher doping concentration, which often involves sophisticated materials design and synthesis (*1*, *40*). Several other strategies have been developed to regulate local heat transfer in photothermal soft actuators, including spatially patterning photothermal agents with selective wavelength to enable localized heating and programmable actuation behaviors (*41*, *42*), and engineered microstructures to steer heat flow and control deformation (*43*). However, these approaches primarily focus on encoding actuation patterns rather than enhancing actuation stroke in thermally dissipative environments. Meanwhile, modulating heat dissipation also plays a crucial role in underwater environments. While external encapsulation has been successfully applied to improve heat accumulation in applications such as greenhouse and solar vapor generation (*44*, *45*), its potential in photothermal actuators remains largely unexplored.

Nature offers a solution to this problem. Amphibious mammals such as otters (*46*), fur seals (*47*), and polar bears (*48*) are able to maintain their body temperature during extended periods underwater thanks to their outstanding thermal insulation (Fig. 1A). This insulation is primarily attributed to their dense and hydrophobic hair, which traps air underwater because of its rough surface nanostructure (*49*). This trapped air layer greatly reduces thermal conductivity, as the heat convection coefficient drops from 100 to 600 W m^{-2} K^{-1} in water to 3 to 20 W m^{-2} K^{-1} in air (*38*). Inspired by this

Department of Material Science and Engineering, University of California, Los Angeles, Los Angeles, CA, USA.
*Corresponding author. Email: chenchi0707@ucla.edu (C.C.); ximinhe@ucla.edu (X.H.)
†These authors contributed equally to this work.

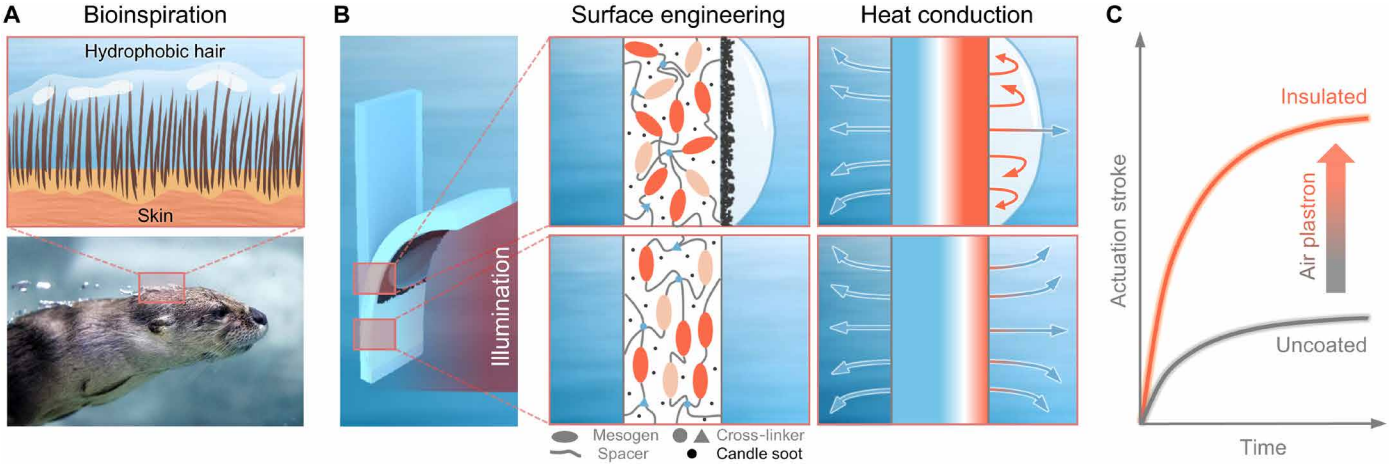

Fig. 1. Scheme of the air plastron–enabled strategy for enhancing the actuation performance of the underwater photothermal soft robot. (**A**) Otter with hydrophobic hair that traps air underwater to help maintain its body temperature. Copyright of the North American River Otter image with permission from D. Strickland, Tennessee Aquarium (*61*). (**B**) The temperature gradient across the thickness of the actuator is enhanced by the candle soot coating that traps air underwater. (**C**) The hydrophobicity of the air plastron leads to better heat insulation on the coated side, leading to a larger actuation stroke.

natural heat insulation strategy, we propose an approach to improve the performance of underwater photothermal actuators by trapping a thin layer of air known as an air plastron on the illuminated side of a photothermal LCE actuator using superhydrophobic candle soot (CS) coating (Fig. 1B). The candle soot coating, characterized by its hierarchical fractal nanostructure, renders the illuminated surface highly hydrophobic (*50*), forming the air plastron as an effective heat insulation layer. Meanwhile, the uncoated side remains in direct contact with water, enabling efficient heat dissipation and rapid thermal relaxation. This design allows for a greater temperature gradient across the thickness of the LCE actuator, which in turn generates a large actuation stroke with a 282-fold improvement in calculated work output to power locomotion (Fig. 1, B and C). Furthermore, we reveal a previously unidentified built-in feedback mechanism enabled by the total internal reflection (TIR) at the bubble-water interface, which decouples the motion direction from the light incidence direction. This contrasts with the conventional self-shadowing mechanism, which requires the motion trajectory to cross over the incident light (*35*, *51*, *52*). As a result, our photo-driven swimmer demonstrates enhanced versatility, achieving horizontal locomotion not only under horizontal light but also with overhead vertical light sources. This improves maneuverability compared to conventional photo-driven robots enabled by self-shadowing that demands the light to strictly align with the locomotion direction (*37*). In summary, this air plastron–enabled strategy participates in the spatiotemporal modulation of heat absorption and dissipation, enabling autonomous cyclic motion with enhanced output performance and introducing expanded functionalities to these soft robotic systems.

RESULTS

To fabricate the photothermal actuator, we synthesized the LCE via a modified two-step thiol-ene Michael addition (*53*), incorporating candle soot dispersed within the matrix as a photothermal agent that strongly absorbs near-infrared irradiation (*50*, *54*). The resulting LCE film exhibited uniaxial contraction when exposed to near-infrared light and reversibly relaxed upon cooling down when the light was off. To effectively trap air underwater for heat insulation, an additional layer of candle soot was coated onto the selected regions of the LCE surface using a modified sprinkle coating method. This process involved first applying a layer of uncured Sylgard 184 diluted with hexanes, followed by drying the hexanes under a flow of air before sprinkling candle soot over the surface. The assembly was then left at room temperature for 24 hours to allow Sylgard 184 to cure and securely adhere to the candle soot (Fig. 2A). The cured Sylgard 184 formed a thin layer of 4.8 μm on average as shown in scanning electron microscopy (SEM) images (fig. S1). The LCE and Sylgard 184 layers exhibited a peel strength of ~0.02 N/mm, indicating strong interfacial adhesion (fig. S2).

To investigate the nanostructure of the soot particles, dynamic light scattering was performed, revealing an average particle size of 17.0 nm, which was confirmed using a transmission electron microscope (fig. S3). Sieved candle soot with a particulate size below 80 μm yielded a coating with the largest water contact angle (WCA) of 150.9°, indicating that the coating was superhydrophobic, while larger particulate sizes slightly decreased the WCA (Fig. 2, B and C). In comparison, an LCE film with only candle soot embedded in the matrix and a blank LCE without any soot content measured 77.5° and 58.7°, respectively, highlighting the essential role of the surface structure in achieving superhydrophobicity. Moreover, the WCA correlated with the surface roughness of the films, as characterized using force profilometry (fig. S4 and Supplementary text S1) and SEM, which revealed the hierarchical fractal-like structure of the candle soot coating consisting of nanoparticles assembled into microscale particulates (Fig. 2D). This structure, resembling the rough surface structure of otter hair, imparted the surface with an extraordinary water-repellent ability (fig. S5) (*46*). As a result, water only wetted the uncoated LCE region, while the air plastron would generate over the coated region that was patterned by selectively applying the Sylgard 184 solution, exhibiting a silver mirror–like appearance underwater because of TIR (Fig. 2E and movie S1) (*55*). Notably, such air plastron remained stable over the timescale of our experiments for more than 180 min at a water depth of 15 cm (fig. S6 and Supplementary text S2). Also, after a water impact test with ~5000 drops of water

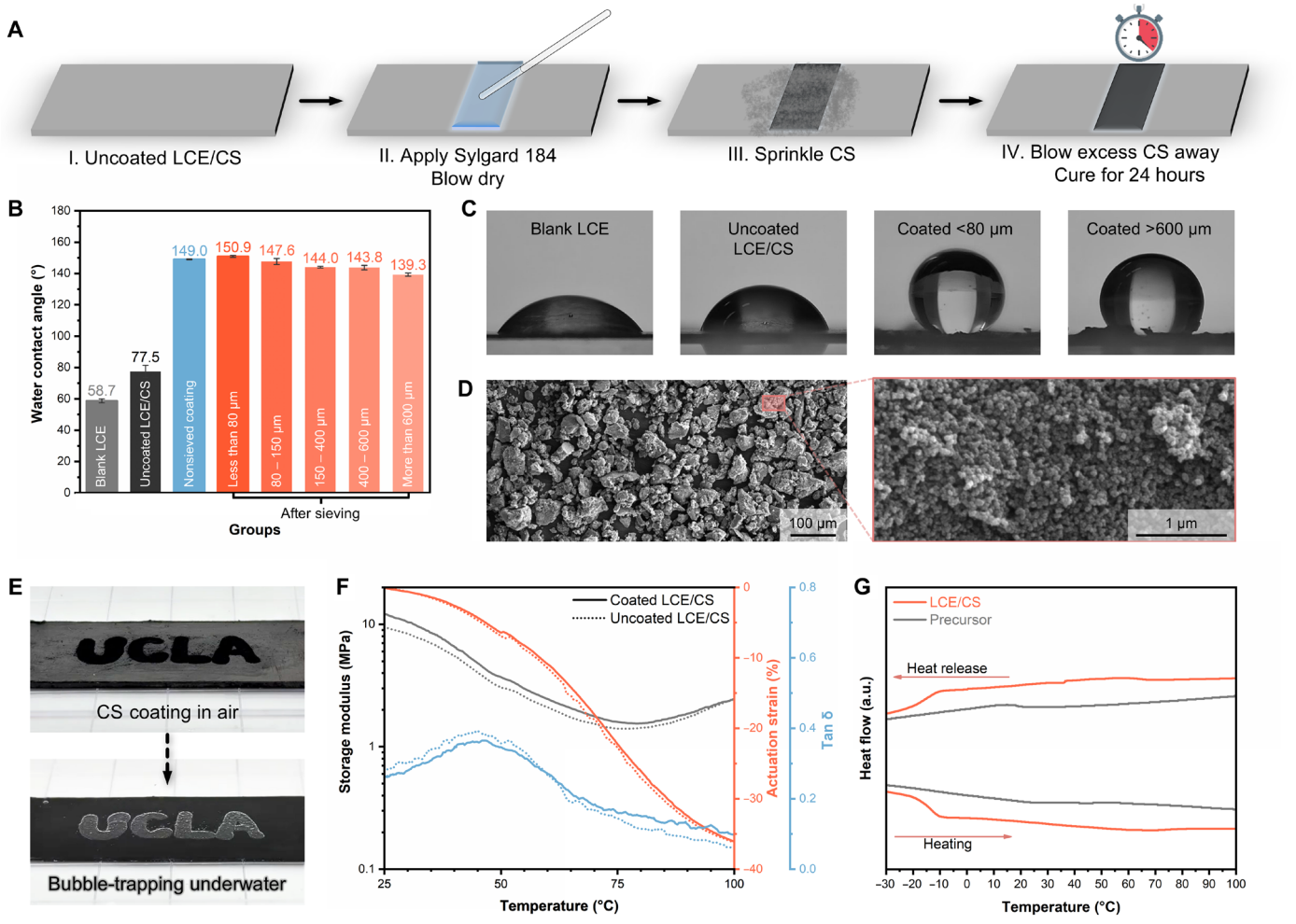

Fig. 2. Fabrication and characterization of the coated LCE film. (**A**) Scheme of a sprinkle coating method to fabricate the coated LCE. CS, candle soot. (**B**) WCA of a blank LCE, uncoated LCE doped with candle soot, and coated LCE with different particulate sizes on the coating. (**C**) Images of water droplets (5 μl) on LCE films with or without coating. (**D**) Top-view SEM images of a coated LCE film (particulate size less than 80 μm) showing the fractal-like structure of the candle soot coating. (**E**) An LCE with candle soot coating in the pattern of "UCLA" was immersed into water, effectively trapping air plastron with a silver mirror–like appearance. (**F**) Comparison of storage moduli, loss tangent, and actuation strain of a coated LCE film and an uncoated LCE film. (**G**) The DSC diagram of the LCE precursor and cross-linked LCE film shows T_{ni} values of 25° and 60°C, respectively. a.u., arbitrary units.

dropping from a height of 20 cm, the WCA at the impact location showed a minimal decrease, suggesting the robustness of the soot coating (fig. S7). Furthermore, because the candle soot coating was sparse, it did not affect the dynamic moduli or actuation strain of LCE (Fig. 2F). Differential scanning calorimetry (DSC) indicated that the candle soot–coated LCE had a low nematic-to-isotropic transition temperature (T_{ni}) of 60°C, which was beneficial for actuation initiation in underwater environments where water convection effectively prevented heat accumulation (Fig. 2G).

To elucidate the underwater actuation mechanism, the LCE film was cut into a simple rectangular geometry (27 mm by 3 mm by 0.14 mm) to facilitate the characterization of autonomous photothermal oscillators based on self-shadowing (*18*, *35*, *37*). For an actuator with a coated area (5 mm by 3 mm), whose lower boundary was 5 mm above the fixed end, when the light intensity increased from 0 to 7.0 W/cm^2, the bending angle kept increasing (i.e., the *y* position of the tip lowered) (Fig. 3A, orange, and movie S2). Simultaneously, the bending motion led to the merging of air trapped on the coating to form a continuous air plastron (fig. S8). Above this threshold, the actuator started to oscillate, with the amplitude and frequency enlarged as the light intensity continued to rise. The tip position of the actuator remained mostly above the laser beam, barely crossing over the irradiation area [Fig. 3, A (red) and C; fig. S9; and movie S3], indicating that the oscillation mechanism was distinct from the previously reported self-shadowing mechanism (*2*, *35*, *51*, *52*), where the tip bent over to block the incident light (Fig. 3B, inner gray loop). In this case, we proposed that the light blocking was caused by TIR at the bubble-water interface. Because the refractive index of water ($n = 1.33$) is higher than that of air ($n = 1.00$), the TIR critical angle is predicted to be 48.6° (*56*). In a simplified model, when the LCE bent to a critical position, the angle between the incident light and the normal increased above the critical angle because of the shape change of the compressed bubble, reducing the transmitted light intensity across the bubble to nearly 0 and therefore allowing the LCE to cool and recover. Consequently, the unbending motion would readmit the incoming light to initiate the next cycle of bending

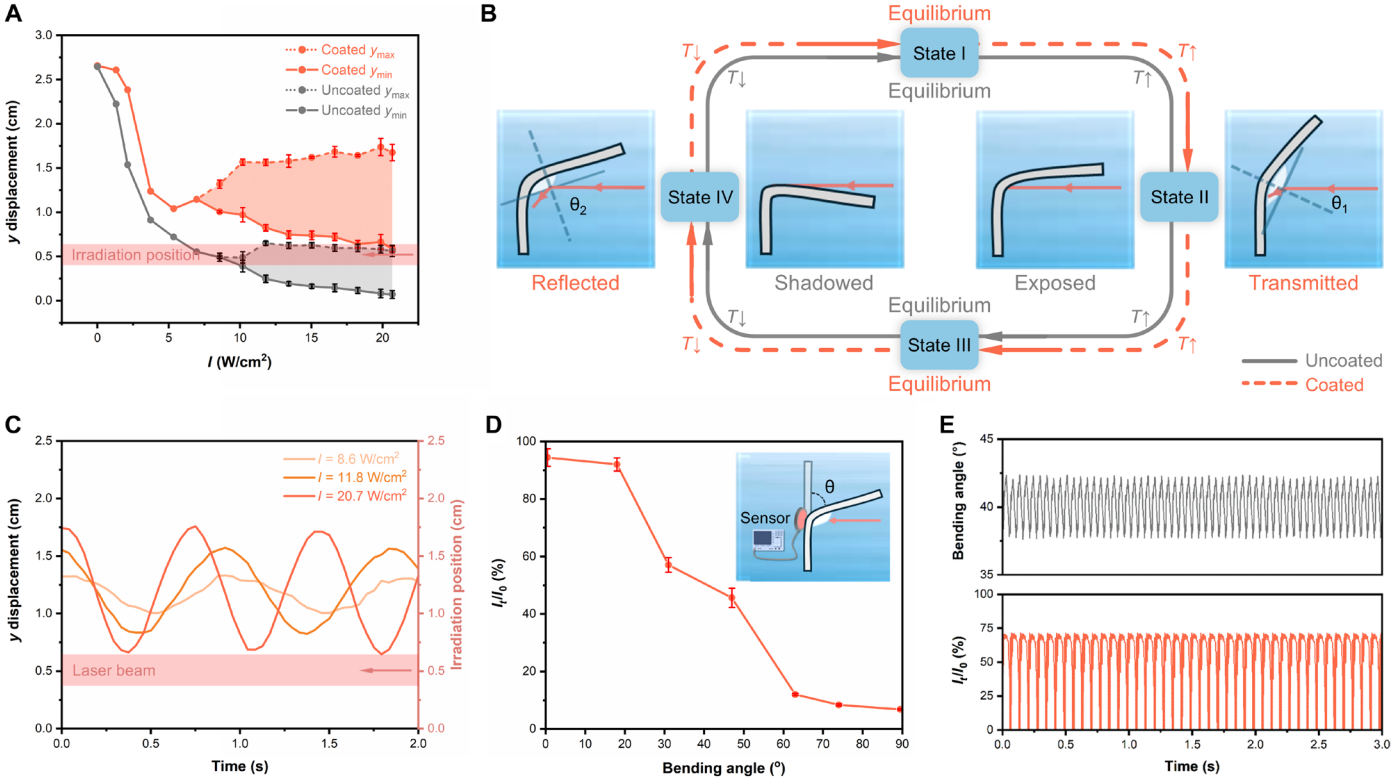

Fig. 3. Oscillation mechanism of the coated underwater actuator with air plastron. (**A**) Oscillation amplitude of coated and uncoated actuators in response to different light intensities. (**B**) Comparison of self-oscillation mechanisms of the coated actuator with air plastron and the uncoated actuator without air plastron. (**C**) Vertical displacement of the coated actuator oscillating above the beam position at different light intensities. (**D**) Fraction of light transmitted across the air plastron at different bending angles of the LCE. (**E**) Simulated bending angle and light transmittance of a coated actuator.

and unbending (Fig. 3B, outer orange loop). Practically, because of the curvature of the bubble and the width of the laser beam, the fraction of light transmitted through the bubble did not exhibit a clean-cut transition between 0 and 100% at a specific bending angle of the LCE. Rather, the fraction of transmitted light decreased gradually with larger bending angles as we compared the light intensity received by the LCE with and without the air plastron. When the LCE was upright (bending angle $\theta = 0°$), nearly 90% of light passed through the air plastron, but it dropped to below 10% when the LCE bent to a position with $\theta > 60°$ (Fig. 3D). In the meantime, a multiphysics model was built to simulate this previously unidentified oscillation behavior of the LCE underwater actuator. The light transmittance can be modeled as follows

$$I_t = I_0 f(\theta), \quad \begin{cases} \theta \le \theta_c, & \text{transmitted} \\ \theta > \theta_c, & \text{total reflected} \end{cases} \tag{1}$$

where θ_c is the critical incident angle of TIR, and $f(\theta) = 1 - R$, with R representing the light reflectance (detailed in Supplementary text S4). TIR occurs when the transmitted angle θ_t reaches $\frac{\pi}{2}$. Therefore, θ_c can be calculated using Snell's law (*57*)

$$n_1 \sin\theta_i = n_2 \sin\theta_t, \quad \theta_c = \arcsin\left(\frac{n_2}{n_1}\right) \tag{2}$$

where n_1 is the refractive index of water, and n_2 is the refractive index of air. I_0 is the initial irradiation power, while I_t is the irradiation power received by the insulated LCE surface after the refraction through the air plastron. This simulation revealed that the variation of light transmittance across the air plastron was in sync with the bending angle during self-oscillation, supporting our hypothesis of TIR-based self-oscillation (Fig. 3E). In comparison, the samples without coating followed the conventional self-shadowing mechanism, where the tip crossed over the laser beam (Fig. 3A, gray).

It is noteworthy that the oscillation amplitude of the coated actuator was notably larger than the uncoated counterpart, and the light intensity threshold for triggering oscillation was also reduced (Fig. 3A). To explore the reason behind the enhanced actuation stroke of the coated actuator, we measured the temperature difference across the thickness (140 μm) in the static state with two ends fixed. For both coated and uncoated actuators, the temperature difference increased with rising light intensity, while the coated actuator always exhibited a greater temperature difference, up to 90.2°C at 20.7 W/cm^2 (Fig. 4A and fig. S10). The reason is explained as follows: When a horizontal beam of the laser irradiated on the LCE through the air plastron, the side facing the laser would be heated to an elevated temperature facilitated by the air insulation, while the opposite side remained in contact with water, efficiently cooling the LCE. Such an asymmetric design thus built a greater temperature gradient across the thickness of the actuator during oscillation (Fig. 1B). This enhanced temperature gradient, in turn, induced a substantial strain difference between the two sides of the LCE, resulting in a large bending moment, as confirmed by COMSOL Multiphysics simulation (Fig. 4, B and C,

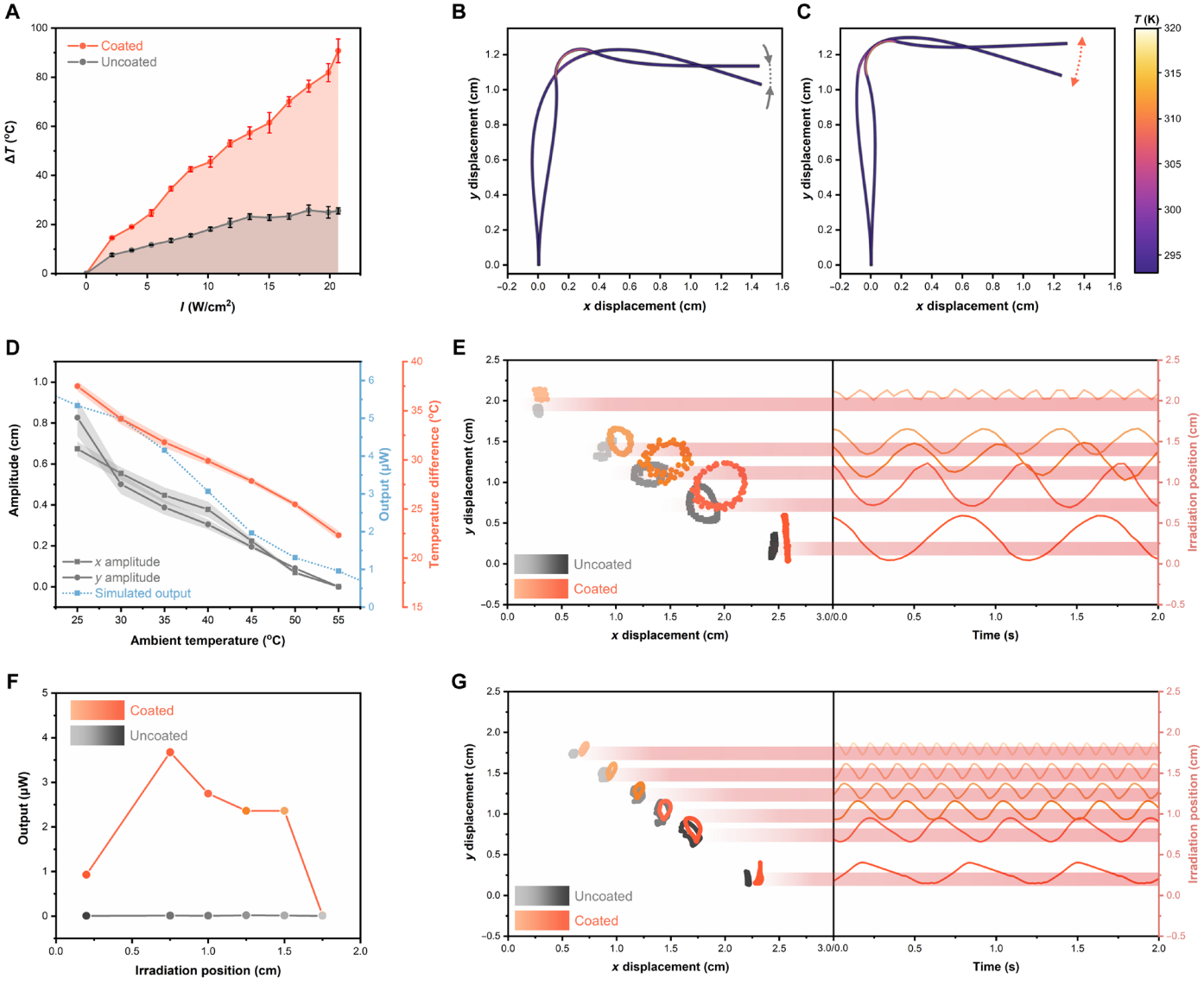

Fig. 4. Oscillation performance of underwater actuators. (**A**) Temperature difference across the thickness of coated and uncoated actuators at different light intensities. Simulated superimposed temperature profile at the highest and lowest positions of (**B**) uncoated and (**C**) coated actuators. (**D**) Oscillation amplitude and simulated work output of a coated actuator at different ambient temperatures. (**E**) Trajectory of the tip motion of coated and uncoated actuators at different irradiation positions at a light intensity of 20.7 W/cm^2. Simulated (**F**) work output and (**G**) trajectory of coated and uncoated actuators.

and Supplementary text S4). The uncoated oscillator and insulated oscillator have different heat transfer functions on the irradiated LCE surface because of their exposure to different heat convection environments (water and air) and the varying photoirradiation power they receive as follows

$$\text{Uncoated oscillator without air plastron: } \rho c_p \frac{\partial T}{\partial t} = k\nabla^2 T - h_w\left(T - T_{\text{env}}\right) + I_0$$
$$\text{Insulated oscillator with air plastron: } \rho c_p \frac{\partial T}{\partial t} = k\nabla^2 T - h_a\left(T - T_{\text{env}}\right) + I_t \quad (3)$$

where ρ is the density of the LCE, c_p is the specific heat capacity of the LCE, k is the thermal conductivity of the LCE, and T_{env} is the environmental temperature. The parameters h_w and h_a are the heat convection coefficients of water and air, respectively. Because of the contribution of air plastron, the effective thermal conductivity of the system was calculated to decrease markedly from 0.7 W m^{-1} K^{-1} for the uncoated LCE to 0.0274 W m^{-1} K^{-1} for the LCE/candle soot/air plastron trilayer (Supplementary text S5), indicating the great effectiveness of the air plastron in inhibiting heat dissipation.

To further investigate the heat transfer process in the actuator with air plastron, we varied the temperature gradient by changing the water temperature from room temperature (25°C) to slightly below its T_{ni} (55°C) (Fig. 4D and fig. S11). At lower temperatures like room temperature, the air plastron effectively facilitated heat build-up on the coated side of the actuator and maintained a considerable temperature gradient across the thickness, thus improving the oscillation

stroke. As the water temperature was raised, the temperature differences between the irradiated position and the surroundings gradually decreased. As a result, the strain difference across the film thickness also decreased substantially despite the larger absolute actuation strain, leading to smaller x and y amplitudes of the tip motion that eventually vanished to zero at 55°C. Meanwhile, the work output of the insulated actuator to the environmental change was simulated, which exhibited a similar decreasing trend with rising water temperature (Fig. 4D, blue), consistent with our experimental observations. These results support the notion that a high temperature gradient is crucial for enhancing the oscillation amplitude and work output of the actuator.

In addition, we compared the trajectory of the tip of the oscillators in response to different irradiation positions. In all cases, the trajectory of coated actuators stayed above that of the uncoated counterparts because of the earlier light blocking via air plastron TIR at smaller bending angles (Fig. 4E). Specifically, when the light irradiated on the root of the actuators (irradiation position of 0 cm), both coated and uncoated samples exhibited reciprocal trajectories, meaning that their upstroke and downstroke followed the same route. However, the coated sample still demonstrated a larger amplitude. At higher irradiation positions, the tip motion had a nonreciprocal circular trajectory, where the spatiotemporal symmetry between the upstroke and the downstroke was broken. Such a nonreciprocal trajectory was generated because the part of the LCE below and above the irradiation position effectively formed a linkage structure that was subject to both the excitation force and drag from the underwater environment, as supported by our multiphysics modeling. Such nonreciprocal motion helped to create a directional imbalance in the distribution of forces and thus generated a net propelling force, particularly in low-Reynolds-number environments where inertia is negligible compared to viscous forces (known as the scallop theorem) (*58*). As a result of the greater oscillation amplitude of the coated actuators, their tips could sweep over a larger area than the uncoated actuators, suggesting potential application in underwater locomotive robots. As the irradiation spot moved further upward, the stiffness of the upper part of the actuator became higher, leading to a decrease in amplitude and an increase in frequency, producing a trajectory with a smaller swept area (fig. S12). Meanwhile, simulations indicated that the coated actuator achieved a work output multiple orders of magnitudes higher than the uncoated sample, reaching a maximum of 282-fold improvement at the height of 0.75 cm (3.67 μW compared to 0.013 μW for the uncoated counterpart) (Fig. 4, F and G). Despite the large actuation stroke, the coating and air plastron were stable during the dynamic oscillation process. Moreover, the oscillation amplitude and frequency remained consistent among different on-off cycles of irradiation (fig. S13) and over a long-term operation of 6 hours (fig. S14), demonstrating the good robustness of this air-plastron-enabled strategy.

As previously mentioned, the large-stroke nonreciprocal motion of a coated actuator with air plastron can potentially generate a propelling force for locomotive robotic applications. To investigate the solid-liquid interaction during the self-oscillation, we performed particle image velocimetry (PIV) to characterize the water flow around the actuator (Fig. 5A, fig. S15, and movie S4). For the coated sample, it could be clearly observed that vortices were generated near the tip of the actuator during its upstroke and downstroke motion. Such features typically yielded a thrust for forward locomotion, seen in the swimming of animals like fish and scallops (*58*). By comparison, an uncoated sample exhibited vorticity of negligible magnitude, which was consistent with its lower oscillation magnitude (Fig. 5B). In addition, the coated actuator also featured a faster updraft heat convection flow than the uncoated actuator, supporting the notion that it reached a higher temperature during oscillation.

Building upon the vortex generation of a coated actuator with air plastron, first, an underwater walking robot was designed to move on a smooth substrate by attaching the oscillating actuator to a polyethylene terephthalate (PET) frame with "legs" (Fig. 5C). The "legs" were tilted such that the friction force in the forward direction (leftward as shown in Fig. 5C) was smaller than that in the backward direction. On the basis of this asymmetric friction force, the underwater walker could move unidirectionally in a pulsatile manner, reaching an average speed of 6 cm/min (0.07 body length/s; Fig. 5D and movie S5). In contrast, the uncoated actuator stayed in the original location as the generated thrust was insufficient to overcome the drag force in the water. To the best of our knowledge, our walker was the only photothermal underwater soft robot achieving autonomous locomotion without the need to manipulate the light source while reaching a swimming speed comparable to that of other underwater swimmers (fig. S16). Similarly, a swimmer at the water-air interface could be designed by having the oscillating actuator function as a paddle that was attached to a hydrophobic acrylic frame that floated on the water surface (leftward as shown in Fig. 5E). A swimming speed of 4.2 cm/min (0.03 body length/s) was achieved for the coated actuator (Fig. 5F and movie S6), while the uncoated actuator could not move forward. In addition, the TIR-based strategy allowed the decoupling of the locomotion direction from the light direction as the LCE actuator did not need to cross over the light beam (fig. S17). Consequently, an underwater walker could be driven by a light source from a variety of angles, ranging from horizontal to overhead, enhancing maneuverability. This feature can be particularly useful in scenarios where direct alignment with the locomotion direction is not feasible or in narrow spaces. In this case, oscillation would occur on one side of the vertical light beam to generate a horizontal thrust that propelled the underwater walker forward (Fig. 5, G and H, and movie S7), demonstrating the potential of autonomous underwater soft robots powered by sunlight-like vertical illumination sources.

DISCUSSION

In this study, we presented an approach to engineering high-performance underwater photothermal actuators by effectively modulating heat transfer processes. Inspired by the thermal insulation strategy of amphibian mammals by trapping air plastrons with their dense, hydrophobic fur, we modulated the heat dissipation of actuators by applying a superhydrophobic material-based coating that facilitated the formation of an insulating air plastron on the LCE actuator. This air plastron strategy offered two major advantages: (i) It maintained a substantial temperature gradient, which in turn drove large actuation strokes and delivered high work output during oscillatory motion; (ii) it introduced a previously unreported mechanism for controlling light interactions in photoactive materials via TIR. Therefore, such a surface engineering approach enabled self-sustained motion even in challenging underwater environments and decoupled the locomotion direction from the light direction. Building on these advances, we successfully fabricated aquatic soft robots capable of

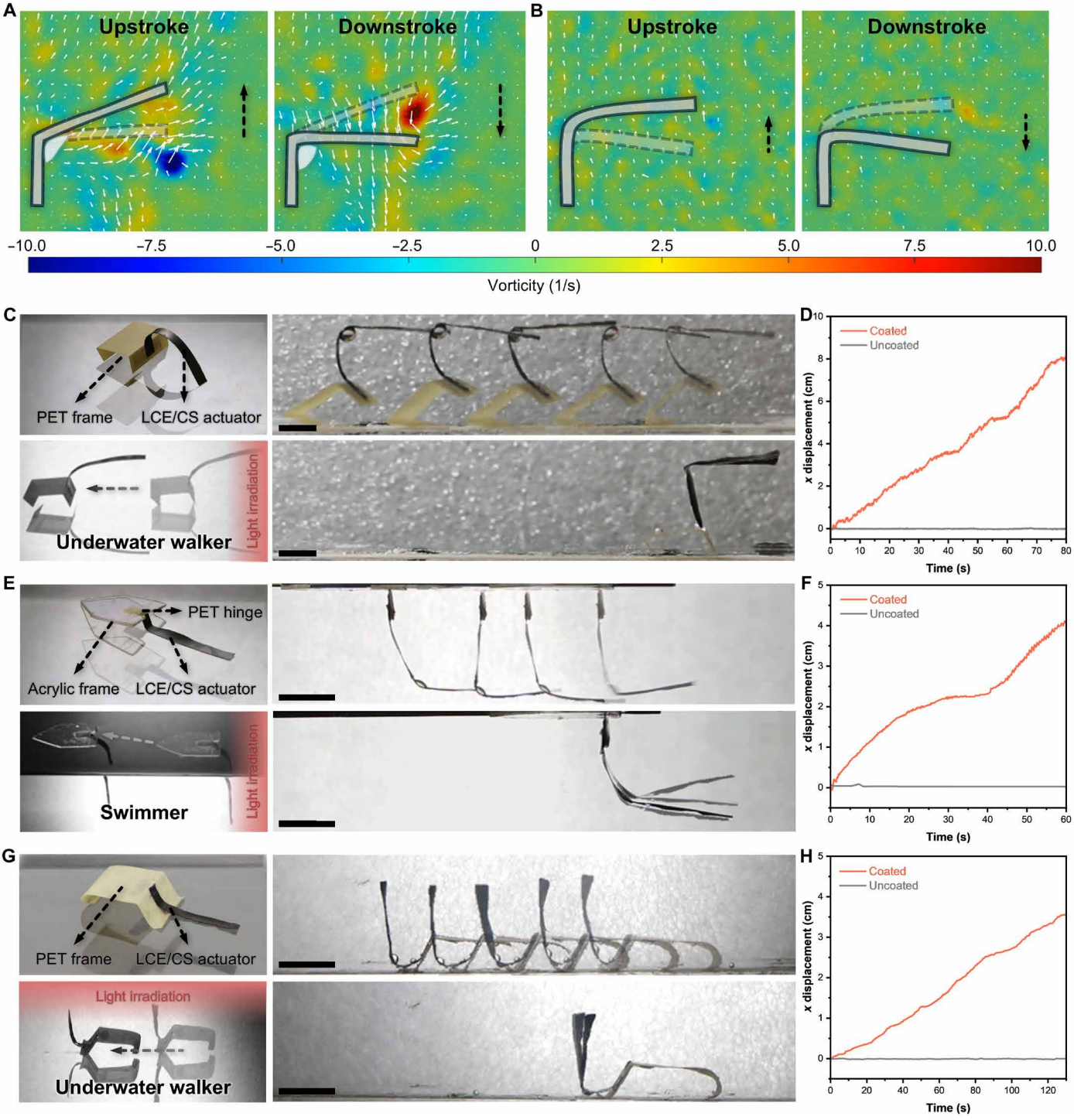

Fig. 5. Locomotive robots based on a coated actuator with air plastron. PIV images presenting (**A**) the coated actuator and (**B**) the uncoated actuator during upstroke and downstroke; color, vorticity; arrow, velocity. (**C**) Underwater walker demonstrating forward movement with a coated actuator while remaining static with an uncoated actuator; scale bars, 1 cm. (**D**) Locomotion performance of the underwater walker. (**E**) Swimmer that moves forward at the water-air interface when using a coated actuator and stays static when using an uncoated actuator; scale bars, 1 cm. (**F**) Locomotion performance of the swimmer. (**G**) Underwater walker demonstrating forward movement with a coated actuator while remaining static with an uncoated actuator under the overhead light irradiation; scale bars, 1 cm. (**H**) Locomotion performance of the underwater walker under the overhead light irradiation.

operating both underwater and at the water surface, driven by both horizontal and overhead vertical light irradiation, demonstrating high locomotion speed up to 0.07 body length/s. Compared to certain stimulus-responsive actuator systems like dielectric actuators and ionic polymer-metal composites or passive pneumatic swimmers, the locomotion speed remains modest. However, many of these systems rely on tethered power supplies—such as high-voltage sources or hydrated electrolytes—that constrain their deployment in fully untethered environments. In contrast, light-responsive LCE enables autonomous actuation by harvesting energy directly from a remote light source, eliminating the need for onboard electronics or external wiring. While further speed optimization is a focus for future work, the demonstrated performance highlights the promise of LCE-based systems for untethered, adaptive applications such as environmental sensing and light-guided navigation.

MATERIALS AND METHODS

Materials

2-Methyl-1,4-phenylene bis(4-(3-(acryloyloxy)propoxy)benzoate) (RM257) and 2-methyl-1,4-phenylene bis(4-((6(acryloyloxy)hexyl) oxy)benzoate) (RM82) were purchased from Shijiazhuang Sdyano Fine Chemical. 1,3,5-Triallyl-1,3,5-triazine-2,4,6(1*H*,3*H*,5*H*)-trione (TATATO), pentaerythritol tetrakis(3-mercaptopropionate) (PETMP), 2-benzyl-2-(dimethylamino)-1-[4-(morpholinyl) phenyl)]-1-butanone (Irgacure 369), butylated hydroxytoluene (BHT), and Tween 80 were purchased from Sigma-Aldrich. Ethylene glycol bis(3-mercaptopropionate) (GDMP) was purchased from TCI. Triethylamine (TEA) was purchased from Merck. Fluorescent particles (UVPMS-BO-1.00 75-90μm) for PIV tests were purchased from Cospheric.

Synthesis of the LCE

To obtain candle soot, a piece of aluminum foil was clamped above the flame of a paraffin candle, and candle soot was scraped off from the aluminum foil. Candle soot particulates of specific size ranges were obtained by sieving the as-prepared candle soot through a series of sieves with mesh sizes of 600, 400, 150, and 80 μm.

The LCE was synthesized using a modified thiol-ene click reaction. Specifically, 103 mg of PETMP, 70 mg of TATATO, 404 mg of GDMP, 24 mg of BHT, 20 mg of Irgacure 369, and 8.5 mg of candle soot were added to a glass vial and mixed thoroughly. Then, 856 mg of RM82 and 250 mg of RM257 were added to the mixture followed by heating at 70°C until it completely melted. The mixture was sonicated while maintaining 70°C for 2 min to disperse the candle soot. Twenty-five microliters of TEA was added to the mixture and stirred for 1 min before casting between two glass slides with two layers of labeling tape as a spacer (280 μm in thickness). The precursor mixture was cured at 60°C for 4 hours to form a lightly cross-linked film. The film was then stretched to 100% strain and photocross-linked under a UV (ultraviolet) lamp at 35 mW cm^{-2} (UVGO 365 nm) for 20 min on each side.

Fabrication of the candle soot–coated oscillator

The LCE film was cut into rectangular strips (27 mm by 3 mm) using a razor blade. Sylgard 184 (10 wt %; base:curing agent = 10:1) was dissolved in hexanes. The solution was spread on the desired area of the LCE strips' surface using a capillary tube before the solvent was dried under a flow of air. Candle soot particulates of specific size ranges were then sprinkled over the strip coated with Sylgard 184, and the strip was gently shaken to ensure that candle soot adhered well to the LCE. Excess candle soot was then blown off from the LCE. The sprinkling and blowing processes were repeated five times to ensure a good coverage of candle soot over Sylgard 184. The coated LCE was kept at room temperature for 24 hours to allow Sylgard 184 to cure.

Characterization of the LCE and candle soot

T_{ni} was measured using a differential scanning calorimeter (DSC250 TA Instruments) by heating 5 to 10 mg of sample from −30° to 100°C at a ramp rate of 10°C min^{-1}. The dynamic moduli and actuation strain of the LCE were measured using a dynamic mechanical analyzer (DMA 850 TA Instruments) by heating from 25° to 140°C at a ramp rate of 5°C min^{-1} under a preload of 0.01 MPa. Specifically, dynamic moduli were tested at a frequency of 1 Hz and an oscillation strain of 0.2%. The WCA was characterized by extruding a water droplet of 5 μl onto the coated/uncoated surface and recording the image using a high-speed camera (VEO-710L, Phantom), and the images were analyzed using the WCA plug-in in ImageJ. Water impact tests were performed by extruding water from a height of 20 cm above an LCE/candle soot film (inclined at 45°) at a constant rate of 10 ml/hour using an electronic pump for a total of 250 ml (~5000 drops), and the WCA before and after the water impact test was recorded (*59*, *60*). The microstructure of the candle soot coating was visualized using a scanning electron microscope (Supra 40VP, ZEISS). The surface roughness of the candle soot coating was measured using a stylus profilometer (6M profilometer, Dektak). Candle soot particles were dispersed in toluene (0.1 mg/ml), and the particle size was measured by dynamic light scattering (Zetasizer Pro, Malvern Panalytical), confirmed by a transmission electron microscope (FEI Titan 80-300). The T-peel test of an LCE/Sylgard 184 bilayer was performed using a tensile tester (Ustretch, Cellscale) at a strain rate of 5 mm min^{-1}. The optical image of air plastron was taken using an optical microscope (VHX-X1F, Keyence).

Actuation and characterization of the oscillator

The LCE oscillator was actuated using a laser at 808 nm (LSR808NL, LASEVER). Light intensity was measured using a power meter (PM16-121, Thorlabs) as the sensor in Fig. 3D. The motion of the oscillator was characterized using Tracker software. To prepare the solution for PIV, 0.1 g of Tween 80 was dissolved in 100 ml of hot water, and 1 g of fluorescent particles was dispersed in the solution by centrifuging at 6000 rpm for 10 min. The mixture was then diluted to 1 liter using deionized water. A line diffuser (ED1-L4100-MD, Thorlabs) was attached to a green laser (Genesis MX532-1000 STM, Coherent) to create a linear green light, which was aligned to the plane of the LCE oscillator to visualize the fluorescent particles. PIV data were analyzed using the Matlab application PIVlab.

Robotic design and characterizations

An underwater walker was fabricated by attaching an LCE/candle soot actuator onto a PET base, which was made by folding a PET film such that the front and rear parts of the base stood tilted toward the same direction on a flat surface (fig. S8). A swimmer was fabricated by attaching an LCE/candle soot actuator onto a PET hinge that was glued onto an acrylic frame. The frame was hydrophobic such that it floats on the water surface. The locomotion of the robots was characterized using Tracker software.

Supplementary Materials

The PDF file includes:

Supplementary Text S1 to S5
Figs. S1 to S17
Legends for movies S1 to S7
References

Other Supplementary Material for this manuscript includes the following:

Movies S1 to S7

REFERENCES AND NOTES

1. L. Dong, Y. Zhao, Photothermally driven liquid crystal polymer actuators. *Mater. Chem. Front.* **2**, 1932–1943 (2018).
2. Y. Zhao, Z. Liu, P. Shi, C. Chen, Y. Alsaid, Y. Yan, X. He, Antagonistic-contracting high-power photo-oscillators for multifunctional actuations. *Nat. Mater.* **24**, 116–124 (2025).
3. Y. Ouyang, G. Huang, J. Cui, H. Zhu, G. Yan, Y. Mei, Advances and challenges of hydrogel materials for robotic and sensing applications. *Chem. Mater.* **34**, 9307–9328 (2022).
4. X. Zhang, B. Tan, Y. Wu, M. Zhang, J. Liao, A review on hydrogels with photothermal effect in wound healing and bone tissue engineering. *Polymers* **13**, 2100 (2021).
5. Y. Hu, Q. Ji, M. Huang, L. Chang, C. Zhang, G. Wu, B. Zi, N. Bao, W. Chen, Y. Wu, Light-driven self-oscillating actuators with phototactic locomotion based on black phosphorus heterostructure. *Angew. Chem.* **133**, 20674–20680 (2021).
6. X. Dong, J. Xu, X. Xu, S. Dai, X. Zhou, C. Ma, G. Cheng, N. Yuan, J. Ding, Sunlight-driven continuous flapping-wing motion. *ACS Appl. Mater. Interfaces* **12**, 6460–6470 (2020).
7. S. Chen, F. Tang, L. Tang, L. Li, Synthesis of Cu-nanoparticle hydrogel with self-healing and photothermal properties. *ACS Appl. Mater. Interfaces* **9**, 20895–20903 (2017).
8. Z. Liu, H. K. Bisoyi, Y. Huang, M. Wang, H. Yang, Q. Li, Thermo- and mechanochromic camouflage and self-healing in biomimetic soft actuators based on liquid crystal elastomers. *Angew. Chem. Int. Ed.* **61**, e202115755 (2022).
9. Y. Wang, J. Wang, L. Huang, X. Ding, Z. Chen, C. Ren, W. Hao, L. Ma, D. Zhang, Photothermally activated self-healing coatings for corrosion protection: A review. *Prog. Org. Coat.* **185**, 107886 (2023).
10. C. Chen, X. Zhao, Y. Chen, W. Chu, Y. Wu, Y. Zhao, P. Shi, W. Chen, H. Li, X. He, H. Liu, Photoinduced dual shape programmability of covalent adaptable networks with remarkable mechanical properties. *Nano Lett.* **22**, 8413–8421 (2022).
11. P. Pallavicini, L. De Vita, F. Merlin, C. Milanese, M. Borzenkov, A. Taglietti, G. Chirico, Suitable polymeric coatings to avoid localized surface plasmon resonance hybridization in printed patterns of photothermally responsive gold nanoinks. *Molecules* **25**, 2499 (2020).
12. H. Kang, J. W. Lee, Y. Nam, Inkjet-printed multiwavelength thermoplasmonic images for anticounterfeiting applications. *ACS Appl. Mater. Interfaces* **10**, 6764–6771 (2018).
13. Y. Ke, J. Chen, G. Lin, S. Wang, Y. Zhou, J. Yin, P. S. Lee, Y. Long, Smart windows: Electro-, thermo-, mechano-, photochromics, and beyond. *Adv. Energy Mater.* **9**, 1902066 (2019).
14. C. Chen, X. Zhao, Y. Chen, X. Wang, Z. Chen, H. Li, K. Wang, X. Zheng, H. Liu, Reversible writing/re-writing polymeric paper in multiple environments. *Adv. Funct. Mater.* **31**, 2104784 (2021).
15. F. Ding, L. Zhang, X. Chen, W. Yin, L. Ni, M. Wang, Photothermal nanohybrid hydrogels for biomedical applications. *Front. Bioeng. Biotechnol.* **10**, 1066617 (2022).
16. G. Xie, X. Wang, M. Mo, L. Zhang, J. Zhu, Photothermal hydrogels for promoting infected wound healing. *Macromol. Biosci.* **23**, 2200378 (2023).
17. Y. Lu, D. Fan, Y. Wang, H. Xu, C. Lu, X. Yang, Surface patterning of two-dimensional nanostructure-embedded photothermal hydrogels for high-yield solar steam generation. *ACS Nano* **15**, 10366–10376 (2021).
18. X. Qian, Y. Zhao, Y. Alsaid, X. Wang, M. Hua, T. Galy, H. Gopalakrishna, Y. Yang, J. Cui, N. Liu, M. Marszewski, L. Pilon, H. Jiang, X. He, Artificial phototropism for omnidirectional tracking and harvesting of light. *Nat. Nanotechnol.* **14**, 1048–1055 (2019).
19. D. Shin, G. Kang, P. Gupta, S. Behera, H. Lee, A. M. Urbas, W. Park, K. Kim, Thermoplasmonic and photothermal metamaterials for solar energy applications. *Adv Opt Mater* **6**, 1800317 (2018).
20. Y. Chen, J. Yang, X. Zhang, Y. Feng, H. Zeng, L. Wang, W. Feng, Light-driven bimorph soft actuators: Design, fabrication, and properties. *Mater. Horiz.* **8**, 728–757 (2021).
21. R. S. Sutar, S. S. Latthe, X. Wu, K. Nakata, R. Xing, S. Liu, A. Fujishima, Design and mechanism of photothermal soft actuators and their applications. *J. Mater. Chem. A* **12**, 17896–17922 (2024).
22. C. Chen, P. Shi, Z. Liu, S. Duan, M. Si, C. Zhang, Y. Du, Y. Yan, T. J. White, R. Kramer-Bottiglio, M. Sitti, T. Iwasaki, X. He, Advancing physical intelligence for autonomous soft robots. *Sci. Robot.* **10**, eads1292 (2025).
23. B. Han, Y.-L. Zhang, L. Zhu, Y. Li, Z.-C. Ma, Y.-Q. Liu, X.-L. Zhang, X.-W. Cao, Q.-D. Chen, C.-W. Qiu, H.-B. Sun, Plasmonic-assisted graphene oxide artificial muscles. *Adv. Mater.* **31**, 1806386 (2019).
24. C. Chen, Y. Liu, X. He, H. Li, Y. Chen, Y. Wei, Y. Zhao, Y. Ma, Z. Chen, X. Zheng, H. Liu, Multiresponse shape-memory nanocomposite with a reversible cycle for powerful artificial muscles. *Chem. Mater.* **33**, 987–997 (2021).
25. L. Liu, J. Wu, B. Chen, J. Gao, T. Li, Y. Ye, H. Tian, S. Wang, F. Wang, J. Jiang, J. Ou, F. Tong, F. Peng, Y. Tu, Magnetically actuated biohybrid microswimmers for precise photothermal muscle contraction. *ACS Nano* **16**, 6515–6526 (2022).
26. J. Li, R. Zhang, L. Mou, M. Jung de Andrade, X. Hu, K. Yu, J. Sun, T. Jia, Y. Dou, H. Chen, S. Fang, D. Qian, Z. Liu, Photothermal bimorph actuators with in-built cooler for light mills, frequency switches, and soft robots. *Adv. Funct. Mater.* **29**, 1808995 (2019).
27. X. Wang, P. Xue, S. Ma, Y. Gong, X. Xu, Polydopamine-modified MXene-integrated poly(*N*-isopropylacrylamide) to construct ultrafast photoresponsive bilayer hydrogel actuators with smart adhesion. *ACS Appl. Mater. Interfaces* **15**, 49689–49700 (2023).
28. X. Li, Y. Du, C. Xiao, X. Ding, X. Pan, K. Zheng, X. Liu, L. Chen, Y. Gong, M. Xue, X. Tian, X. Zhang, Tendril-inspired programmable liquid metal photothermal actuators for soft robots. *Adv. Funct. Mater.* **34**, 2310380 (2024).
29. S. Li, Z. Cai, J. Han, Y. Ma, Z. Tong, M. Wang, L. Xiao, S. Jia, X. Chen, Fast-response photothermal bilayer actuator based on poly(*N*-isopropylacrylamide)–graphene oxide–hydroxyethyl methacrylate/polydimethylsiloxane. *RSC Adv.* **13**, 18090–18098 (2023).
30. W. Liu, Z. Lei, W. Xing, J. Xiong, Y. Zhang, P. Tao, W. Shang, B. Fu, C. Song, T. Deng, Enable multi-stimuli-responsive biomimetic actuation with asymmetric design of graphene-conjugated conductive polymer gradient film. *ACS Nano* **17**, 16123–16134 (2023).
31. Y. Bai, J. Zhang, D. Wen, B. Yuan, P. Gong, J. Liu, X. Chen, Fabrication of remote controllable devices with multistage responsiveness based on a NIR light-induced shape memory ionomer containing various bridge ions. *J. Mater. Chem. A* **7**, 20723–20732 (2019).
32. Y. Zheng, C. Li, Photothermally-driven oxazine hydrogel actuators at the water-air interface. *Giant* **16**, 100192 (2023).
33. H. Tian, Z. Wang, Y. Chen, J. Shao, T. Gao, S. Cai, Polydopamine-coated main-chain liquid crystal elastomer as optically driven artificial muscle. *ACS Appl. Mater. Interfaces* **10**, 8307–8316 (2018).
34. B. Lei, Z.-Y. Wen, H.-K. Wang, J. Gao, L.-J. Chen, Bioinspired jumping soft actuators of the liquid crystal elastomer enabled by photo-mechanical coupling. *ACS Appl. Mater. Interfaces* **16**, 1596–1604 (2024).
35. Y. Zhao, Q. Li, Z. Liu, Y. Alsaid, P. Shi, M. Khalid Jawed, X. He, Sunlight-powered self-excited oscillators for sustainable autonomous soft robotics. *Sci. Robot.* **8**, eadf4753 (2023).
36. H. Shahsavan, A. Aghakhani, H. Zeng, Y. Guo, Z. S. Davidson, A. Priimagi, M. Sitti, Bioinspired underwater locomotion of light-driven liquid crystal gels. *Proc. Natl. Acad. Sci. U.S.A.* **117**, 5125–5133 (2020).
37. Y. Zhao, C. Xuan, X. Qian, Y. Alsaid, M. Hua, L. Jin, X. He, Soft phototactic swimmer based on self-sustained hydrogel oscillator. *Sci. Robot.* **4**, eaax7112 (2019).
38. R. B. Bird, Transport phenomena. *Appl. Mech. Rev.* **55**, R1–R4 (2002).
39. N. P. Pinchin, H. Guo, H. Meteling, Z. Deng, A. Priimagi, H. Shahsavan, Liquid crystal networks meet water: It's complicated! *Adv. Mater.* **36**, 2303740 (2024).
40. X. Cui, Q. Ruan, X. Zhuo, X. Xia, J. Hu, R. Fu, Y. Li, J. Wang, H. Xu, Photothermal nanomaterials: A powerful light-to-heat converter. *Chem. Rev.* **123**, 6891–6952 (2023).
41. A. S. Kuenstler, Y. Chen, P. Bui, H. Kim, A. DeSimone, L. Jin, R. C. Hayward, Blueprinting photothermal shape-morphing of liquid crystal elastomers. *Adv. Mater.* **32**, 2000609 (2020).
42. E. Oh, Y. Lee, H.-J. Lee, Y. Na, A. Kim, J. D. Park, C. Yoon, S. H. Song, Untethered wavelength-selective multi-shape programmable hybrid soft robot. *Sci. Rep.* **15**, 9240 (2025).
43. X. Li, Y. Du, X. Pan, C. Xiao, X. Ding, K. Zheng, X. Liu, L. Chen, Y. Gong, M. Xue, X. Tian, X. Zhang, Leaf vein-inspired programmable superstructure liquid metal photothermal actuator for soft robots. *Adv. Mater.* **37**, 2416991 (2025).
44. L. Zhu, T. Ding, M. Gao, C. K. N. Peh, G. W. Ho, Shape conformal and thermal insulative organic solar absorber sponge for photothermal water evaporation and thermoelectric power generation. *Adv. Energy Mater.* **9**, 1900250 (2019).
45. M. Fang, Q. Li, D. Yang, B. Zhou, Y. Feng, C. Liu, Synergistic light-to-heat conversion effect of MXene-based transparent film with insulating PDMS/Fe_3O_4 coating. *Compos. Part A Appl. Sci. Manuf.* **174**, 107745 (2023).
46. J. W. Weisel, C. Nagaswami, R. O. Peterson, River otter hair structure facilitates interlocking to impede penetration of water and allow trapping of air. *Can. J. Zool.* **83**, 649–655 (2005).
47. H. E. M. Liwanag, A. Berta, D. P. Costa, M. Abney, T. M. Williams, Morphological and thermal properties of mammalian insulation: The evolution of fur for aquatic living. *Biol. J. Linn. Soc.* **106**, 926–939 (2012).
48. W.-H. Zhu, S.-T. Zhang, Z.-B. Li, An analysis of heat conduction in polar bear hairs using one-dimensional fractional model. *Therm. Sci.* **20**, 785–788 (2016).
49. Z. Shao, Y. Wang, H. Bai, A superhydrophobic textile inspired by polar bear hair for both in air and underwater thermal insulation. *Chem. Eng. J.* **397**, 125441 (2020).
50. S. Wu, Y. Du, Y. Alsaid, D. Wu, M. Hua, Y. Yan, B. Yao, Y. Ma, X. Zhu, X. He, Superhydrophobic photothermal icephobic surfaces based on candle soot. *Proc. Natl. Acad. Sci. U.S.A.* **117**, 11240–11246 (2020).
51. S. Serak, N. Tabiryan, R. Vergara, T. J. White, R. A. Vaia, T. J. Bunning, Liquid crystalline polymer cantilever oscillators fueled by light. *Soft Matter* **6**, 779–783 (2010).

52. A. H. Gelebart, G. Vantomme, E. W. Meijer, D. J. Broer, Mastering the photothermal effect in liquid crystal networks: A general approach for self-sustained mechanical oscillators. *Adv. Mater.* **29**, 1606712 (2017).
53. M. O. Saed, C. P. Ambulo, H. Kim, R. De, V. Raval, K. Searles, D. A. Siddiqui, J. M. O. Cue, M. C. Stefan, M. R. Shankar, T. H. Ware, Molecularly-engineered, 4D-printed liquid crystal elastomer actuators. *Adv. Funct. Mater.* **29**, 1806412 (2019).
54. P. Shi, Y. Zhao, Z. Liu, X. He, Liquid crystal elastomer composite-based photo-oscillator for microrobots. *J. Compos. Mater.* **57**, 633–643 (2023).
55. J. Lee, K. Yong, Surface chemistry controlled superhydrophobic stability of W 18 O 49 nanowire arrays submerged underwater. *J. Mater. Chem.* **22**, 20250–20256 (2012).
56. E. Passaglia, R. R. Stromberg, Optical properties of thin films on transparent surfaces by ellipsometry; Internal reflection for film covered surfaces near the critical angle. *J. Res. Natl. Bur. Stand. A Phys. Chem.* **68A**, 601–610 (1964).
57. E. Stachura, "Fermat principle and Snell's law of refraction" in *Mathematical Methods in Liquid Crystal Optics and Lens Design*, E. Stachura, Ed. (Springer Nature Switzerland, 2024), pp. 61–91.
58. M. Hubert, O. Trosman, Y. Collard, A. Sukhov, J. Harting, N. Vandewalle, A.-S. Smith, Scallop theorem and swimming at the mesoscale. *Phys. Rev. Lett.* **126**, 224501 (2021).
59. T. F. Qahtan, M. A. Gondal, I. O. Alade, M. A. Dastageer, Fabrication of water jet resistant and thermally stable superhydrophobic surfaces by spray coating of candle soot dispersion. *Sci. Rep.* **7**, 7531 (2017).
60. N. Celik, N. B. Kiremitler, M. Ruzi, M. S. Onses, Waxing the soot: Practical fabrication of all-organic superhydrophobic coatings from candle soot and carnauba wax. *Prog. Org. Coat.* **153**, 106169 (2021).
61. Tennessee Aquarium, North American River Otter (2020); https://tnaqua.org/animal/north-american-river-otter/.
62. The Engineering ToolBox, "Air properties - Density, viscosity, heat capacity, thermal conductivity, and more" (2003); www.engineeringtoolbox.com/air-properties-d_156.html.
63. C. Ahn, K. Li, S. Cai, Light or thermally powered autonomous rolling of an elastomer rod. *ACS Appl. Mater. Interfaces* **10**, 25689–25696 (2018).
64. C. Huang, J. Lv, X. Tian, Y. Wang, Y. Yu, J. Liu, Miniaturized swimming soft robot with complex movement actuated and controlled by remote light signals. *Sci. Rep.* **5**, 17414 (2015).
65. S. Palagi, A. G. Mark, S. Y. Reigh, K. Melde, T. Qiu, H. Zeng, C. Parmeggiani, D. Martella, A. Sanchez-Castillo, N. Kapernaum, F. Giesselmann, D. S. Wiersma, E. Lauga, P. Fischer, Structured light enables biomimetic swimming and versatile locomotion of photoresponsive soft microrobots. *Nat. Mater.* **15**, 647–653 (2016).
66. K. Y. Lee, S.-J. Park, D. G. Matthews, S. L. Kim, C. A. Marquez, J. F. Zimmerman, H. A. M. Ardoña, A. G. Kleber, G. V. Lauder, K. K. Parker, An autonomously swimming biohybrid fish designed with human cardiac biophysics. *Science* **375**, 639–647 (2022).
67. S.-J. Park, M. Gazzola, K. S. Park, S. Park, V. Di Santo, E. L. Blevins, J. U. Lind, P. H. Campbell, S. Dauth, A. K. Capulli, F. S. Pasqualini, S. Ahn, A. Cho, H. Yuan, B. M. Maoz, R. Vijaykumar, J.-W. Choi, K. Deisseroth, G. V. Lauder, L. Mahadevan, K. K. Parker, Phototactic guidance of a tissue-engineered soft-robotic ray. *Science* **353**, 158–162 (2016).

Acknowledgments: We thank D. Strickland and Tennessee Aquarium for providing the images of Sunshine, the North American river otter, featured in Fig. 1A. **Funding:** This work is supported by grants received by X.H. from the Johnson & Johnson WISTEM^{2}D Scholar award, the American Chemical Society (GR-63402), the Office of Naval Research (ONR) awards (N000142412187 and N000142212595), and the Moore Foundation Award (12072).
Author contributions: Conceptualization: P.S., C.C., and X.H. Methodology: P.S., C.C., and W.H. Formal analysis: C.C., Z.W., and Z.L. Software: Z.W. and Z.L. Data curation: P.S., C.C., M.S., and X.H. Validation: P.S., C.C., Z.W., W.H., and M.S. Investigation: P.S., C.C., W.H., M.S., Z.L., W.H., and C.Z. Visualization: P.S., C.C., and S.D. Supervision: C.C. and X.H. Resources: C.C. and X.H. Funding acquisition: X.H. Writing—original draft: P.S., C.C., and X.H. Writing—review and editing: all authors. Project administration: C.C. and X.H. **Competing interests:** The authors declare that they have no competing interests. **Data and materials availability:** All data needed to evaluate the conclusions in the paper are present in the paper and/or the Supplementary Materials.

Submitted 29 March 2025
Accepted 11 July 2025
Published 15 August 2025
10.1126/sciadv.adx7189